Quantification of Underwater Sargassum Aggregations Based on a Semi-Analytical Approach Applied to Sentinel-3/OLCI (Copernicus) Data in the Tropical Atlantic Ocean

Léa Schamberger, Audrey Minghelli, Malik Chami

remote sensing

MDPI

Article

Quantification of Underwater *Sargassum* Aggregations Based on a Semi-Analytical Approach Applied to Sentinel-3/OLCI (Copernicus) Data in the Tropical Atlantic Ocean

Léa Schamberger [1,2], Audrey Minghelli [1,2,*] and Malik Chami [3]

[1] Laboratoire d'Informatique et Système (LIS), Université de Toulon, CNRS UMR 7020, F-83041 Toulon, France
[2] Laboratoire d'Informatique et Système (LIS), Aix Marseille Université, F-13288 Marseille, France
[3] Laboratoire Atmosphères Milieux Observations Spatiales (LATMOS), Sorbonne Université, CNRS-INSU, F-06304 Nice, France
* Correspondence: audrey.minghelli@univ-tln.fr

Abstract: "*Sargassum*" is a pelagic species of algae that drifts and aggregates in the tropical Atlantic Ocean. The number of *Sargassum* aggregations increased in the Caribbean Sea during the last decade. The aggregations eventually wash up on shores thus leading to a socio-economic issue for the population and the coastal ecosystem. Satellite ocean color data, such as those provided by the Sentinel-3/OLCI satellite sensor (Copernicus), can be used to detect the occurrences of *Sargassum* and to estimate their abundance per pixel using the Maximum Chlorophyll *Index* (noted MCI). Such an index is, however, ineffective if the algae are located beneath the sea surface, which frequently happens, considering the rough Caribbean oceanic waters. The objective of this study is to propose a relevant methodology that enables the detection of underwater *Sargassum* aggregations. The methodology relies on the inversion of the radiative transfer equation in the water column. The inverted model provides the immersion depth of the *Sargassum* aggregations (per pixel) and their fractional coverage from the above water reflectances. The overall methodology has been applied to Sentinel-3/OLCI data. The comparison with the MCI method, which is solely devoted to the sea surface retrieval of *Sargassum* aggregations, shows that the proposed methodology allows retrieving about twice more *Sargassum* aggregation occurrences than the MCI estimates. A relative increase of 31% of the fractional coverage over the entire study area is observed when using the proposed method in comparison to MCI method. For the satellite scenes considered here, the rate of *Sargassum* aggregations immersed between 2 m and 5 m depth ranges between 30% and 51% over the total amount (i.e., surface + in-water), which clearly demonstrates the importance of considering the retrieval of in-water aggregations to gain understanding on *Sargassum* spatial variability in the oceanic and coastal ecosystems.

Keywords: *Sargassum* aggregations; ocean color remote sensing; Sentinel-3/OLCI satellite sensor; radiative transfer modelling; tropical Atlantic Ocean

Citation: Schamberger, L.; Minghelli, A.; Chami, M. Quantification of Underwater *Sargassum* Aggregations Based on a Semi-Analytical Approach Applied to Sentinel-3/OLCI (Copernicus) Data in the Tropical Atlantic Ocean. *Remote Sens.* **2022**, *14*, 5230. https://doi.org/10.3390/rs14205230

Academic Editors: Stefano Vignudelli, Jorge Vazquez, Emmanuel Devred, Cédric Jamet and Oleg Kopelevich

Received: 17 August 2022
Accepted: 15 October 2022
Published: 19 October 2022

1. Introduction

The *Sargassum* is a species of algae originally found in the "Sargasso Sea", which is located in the northwestern region of the tropical Atlantic Ocean offshore the Florida coastlines (USA). In the last decade, *Sargassum* has be observed in large amounts from the Caribbean Sea to Brazil and could extend up to the coastlines of the north-west of Africa [1]. Such a shift in the *Sargassum* spatial distribution, which was observed in 2011 by Gower et al. [2], can be ascribed to both global change, particularly the water warming, and to the nutrient supply caused by farming [3]. The *Sargassum* are transported by the currents and winds until they wash up on shores. Two pelagic species of *Sargassum*, namely *S. natans* and *S. fluitans*, are prevailing in beaching events. Those species have a key role in the ecosystem by providing habitats and by sequestrating carbon [4,5]. However, the

decomposition of such algae generates Hydrogen Sulfide (H_2S) gas which releases a "rotten egg" odor and can impact inhabitants' health. The strong increase in the beaching events also impacts the tourism and the coastal environment [1]. The biological properties of *Sargassum* have been recently investigated to better understand their formation, aggregation and life cycle [6,7]. Satellite remote sensing observations are relevant assets to provide a wide spatial and temporal extent of the *Sargassum* distribution at synoptic scale.

The first spectral index, namely the Maximum Chlorophyll Index (MCI), was proposed by Gower et al. to detect intense plankton bloom [8] and *Sargassum* aggregations [9,10] using MERIS data. This index is based on a linear combination of three spectral bands of MERIS sensor in the near infrared (NIR) domain. This is because the *Sargassum* reflectance shows a strong increase in the red-edge and near NIR parts of the spectrum similarly as it could be observed for land vegetation spectral features (see Figure 2 in [10]). The water leaving reflectance spectrum is then characterized by a pronounced signature in those spectral domains for *Sargassum* dominated waters. The identification (or detection) of *Sargassum* from remotely sensed data acquired over the open ocean currently relies on such a spectral signature. MCI was further adjusted to be applied to the satellite sensor "Ocean Land Color Imager (OLCI)" onboard Sentinel-3 [11]. Hu proposed another spectral index, the Floating Algae Index (FAI) [12], using MODIS sensor to detect *Sargassum*. One limitation of FAI index is that it could also be an indicator of the presence of clouds, particularly for high FAI values, which can make it challenging to quantify the actual coverage of *Sargassum* in the open ocean. Wang and Hu [13] improved the FAI index by proposing an Alternative Floating Algae Index (AFAI), which is supposed to be less sensitive to the presence of clouds. They were able to estimate the abundance of *Sargassum* in the Gulf of Mexico. Wang and Hu [13] developed an approach to determine the coverage of *Sargassum* per pixels (i.e., their abundance) based on a linear relationship between the fractional coverage (FC) and the AFAI index [14]. FC is defined as the ratio (in %) between the surface area of *Sargassum* aggregation within one pixel and the total surface area of that pixel. The biomass quantity of Sargassum within a pixel can be estimated using a relationship defined empirically by [15] between the fractional coverage, the pixel size resolution and a calibration constant which value is 3.34 kg m^{-2}. The correct estimation of the fractional coverage from remote sensing data is then crucial to determine the amount of Sargassum biomass in the ocean and to improve the strandings forecast of Sargassum in coastal zones. Recently, neural network approaches were implemented to detect the presence of *Sargassum* in the open ocean. [16]. Other deep learning approaches use expert visualization of the red color in composite images for the training phase to provide *Sargassum* occurrences (ERIS-NET, [17]). The asset of such methods is to take into account the full spectrum of reflectance instead of focusing only on the red-edge and NIR domains.

Sargassum aggregations are often subject to move at depths greater than 1 m as a result of the wind (>4 m/s) and of the roughness of the sea in Caribbean waters [18]. When the *Sargassum* are immersed in the water column, the above water reflectance red edge/NIR peak is strongly attenuated as a result of the high pure seawater absorption coefficient in these spectral bands. Therefore, the performance of the current *Sargassum* algal detection indexes, which are all based on red-edge/NIR bands, could significantly decrease, thus making more challenging the detection *Sargassum* of aggregations present in the ocean [19]. The originality of the current study is to take into account the immersion depth of *Sargassum* for improving their detection from satellite and for estimating their fractional coverage.

Lee et al. [20] proposed a direct semi-analytical radiative transfer model in shallow waters that is able to simulate the water leaving reflectance from the bio-optical properties, depth, and benthic habitat composition. Descloitres et al. [21] recently adapted the Lee's model to analyze the influence of immersion depth and fractional coverage on the surface reflectance. Since the semi-analytical Lee's model can be inverted, it will be used here to retrieve the *Sargassum* aggregation parameters, especially *Sargassum* depth and fractional coverage, from the surface reflectance derived from Sentinel-3/OLCI observations.

The paper is organized as follows: the study area in the Caribbean Sea, the Sentinel-3/OLCI satellite data and the methodology used to estimate in-water and surface *Sargassum* aggregation properties are described Section 2. The performances of the methodology and the application to Sentinel-3/OLCI data are outlined Section 3. The implementation of a neural network approach for reducing the computational time for processing a large OLCI dataset is presented in Section 4. Finally, the comparison of the proposed approach with a standard surface *Sargassum* detection method is discussed in Section 5.

2. Materials and Methods

2.1. Study Area

The area of interest is located in the Caribbean Sea between 6°N and 16°N latitudes and between 58°W and 63°W longitudes (Figure 1). The red square in Figure 1 focuses on the spatial location of the studied zone (Lesser Antilles). This zone is about 2 million km^2 which is similar to the spatial coverage of a typical OLCI satellite image (i.e., 1227 km × 1460 km) (Figure 2).

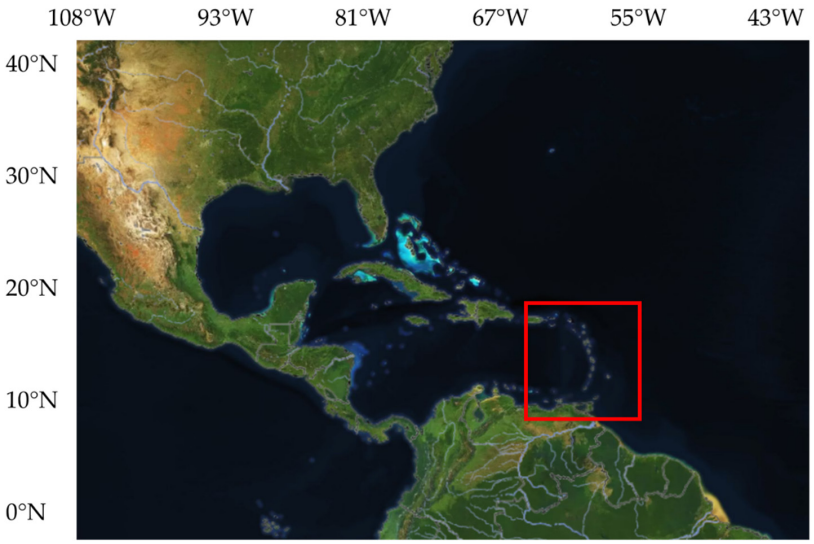

Figure 1. General overview of the area of interest in the Caribbean Sea (red square).

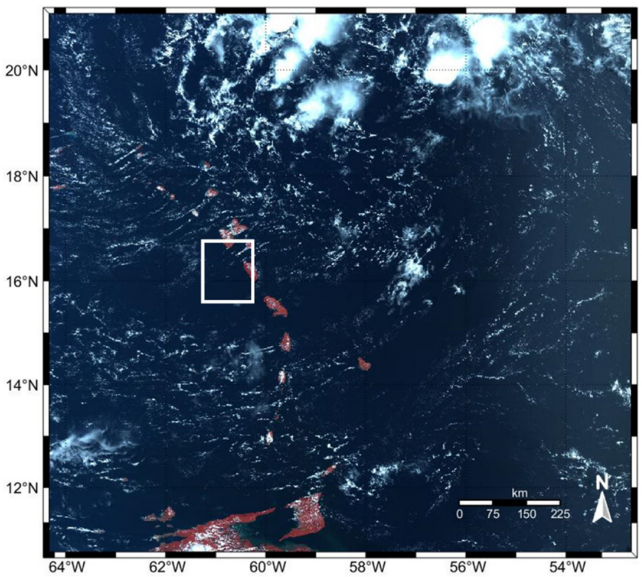

Figure 2. False color composite (NIR Green Blue bands) of the OLCI image acquired on 8 July 2017, 13:55 (UTC); the white square shows the regional study area in the west of Dominica.

2.2. Satellite Data

The Sentinel-3/OLCI sensor is used in this study for the detection and quantification of *Sargassum* over the study area. OLCI sensor acquires data for 21 bands spectral resolution at a spatial resolution of 300 m and a temporal revisit of two days with the two-satellite constellations [22]. Its Signal-to-Noise Ratio (SNR) ranges from 2188 to 152 from 400 nm to 1020 nm bands, respectively, thus allowing the acquisition of high radiometric quality data over dark waters such as those encountered in the open ocean. The dataset used in this study consists of seven images that were acquired on the following dates: 8 July 2017, 13:55 (UTC); 27 May 2018, 14:21; 14 June 2020 14:02; 14 September 2020 14:17; 28 December 2020 13:55; and finally, 2 May 2021, 14:15. Those scenes were selected because they exhibit significant occurrences of *Sargassum* and also because they were acquired at various seasons and for different years. The Level-1 data product, namely the top-of-atmosphere radiance (TOA), were downloaded from the European Copernicus platform [23]. As an example, a false color composite (NIR-Green-Blue) image acquired on 8 July 2017, 13:55, is shown Figure 2. The regional study area that is analyzed in this paper, is west of Dominica Island (see the white square in Figure 2). Such an area covers 22,500 km^2.

2.3. Methodology

2.3.1. Atmospheric Correction Procedure over Sargassum Dominated Waters

The first requirement for the detection of in-water *Sargassum* aggregations is to derive the water leaving reflectance at the sea surface level from satellite data. Thus, the top of the atmosphere (TOA) reflectance (ρ_{TOA}) needs to be corrected for the atmospheric effects such as the Rayleigh (i.e., molecular) and aerosols scattering and sun/sky glint. While the Rayleigh atmospheric scattering is known from theory, the estimation of the aerosol reflectance remains challenging due to the high variability in their spatial and optical properties [24]. The POLYMER atmospheric correction algorithm [25] could be used to retrieve the above water reflectance over open ocean waters. POLYMER was first applied to ENVISAT/MERIS data and more recently to Sentinel-2/MSI and Sentinel-3/OLCI data [26,27]. POLYMER atmospheric correction approach firstly consists in normalizing the TOA radiance by the cosine of the solar zenithal angle (θ_w) and the extraterrestrial solar irradiance (Es) to obtain the TOA reflectances (ρ_{TOA}). ρ_{TOA} can then be decomposed as follows (Equation (1)):

$$\rho_{TOA} = t_{oz}t_{NO2}\left(\rho_{mol} + T\rho_{gli} + \rho_{aer} + \rho_{coupl} + t\rho_w^+\right) \quad (1)$$

where t_{oz} and t_{NO2} are, respectively, the transmittance of the ozone and the nitrogen dioxide, ρ_{mol} accounts for the Rayleigh molecular scattering, ρ_{gli} is the sunglint reflectance, T is the direct transmittance, ρ_{aer} is the reflectance of the aerosols, ρ_{coupl} represents various coupling terms between the sunglint, the molecules and the aerosols, t is the total (i.e., direct and diffuse) transmittance for atmospheric scattering, and finally, ρ_w^+ is the sea surface reflectance (i.e., above water reflectance). The top of the atmosphere reflectance is first corrected for the ozone transmittance, the Rayleigh scattering effects and most of the sunglint reflectance (Cox and Munk (1954, [28]) which are known from theoretical calculations. The derived reflectance is called ρ'. The reflectance ρ' can be expressed from Equation (1) as follows Equation (2) where ρ_{ag} includes the aerosols reflectance, the coupling term.

$$\rho'(\lambda) = \rho_{ag}(\lambda) + t(\lambda)\rho_w^+(\lambda) \quad (2)$$

POLYMER then relies on the expression of the term ρ_{ag} as a polynomial function of λ and ρ_{mol} (Equation (3)):

$$\rho_{ag}(\lambda) = t_0c_0 + c_1\lambda^{-1} + c_2\rho_{mol} \quad (3)$$

A least square fitting approach on the satellite measurements is then applied to estimate ρ_{ag}. The intrinsic *Sargassum* reflectance exhibits a strong increase in the near infrared (NIR) (see Figure 2 in [10]). Such an increase remains significant enough to influence

the overall oceanic reflectance although the fractional *Sargassum* coverage that is usually encountered in the ocean is weak; typically lower than 5% based on MODIS data [13]. However, since the *Sargassum* intrinsic reflectance is not considered by the POLYMER algorithm, the *Sargassum* optical signature on the top of atmosphere reflectance is wrongly identified as an aerosol signature. This leads to an overestimation of the reflectance ρ_{ag} in the NIR domain and the subsequent loss of the *Sargassum* signature on the total surface reflectance (ρ_w^+) (see Figure 4 in [29]).

Schamberger et al. [29] recently addressed the issue of correcting ρ_{TOA} for atmospheric effects over *Sargassum* dominated waters by adjusting the POLYMER algorithm, hereafter noted $POLYMER_{ext,}$ to the presence of *Sargassum*. $POLYMER_{ext}$ is thus used here to derive the sea surface reflectance. Briefly, $POLYMER_{ext}$ consists in first determining the effect of the Rayleigh scattering. Second, the aerosol and sunglint reflectances are estimated over *Sargassum*-free pixels based on the NIR bands. Third, the estimation of aerosol/sunglint reflectances is performed over *Sargassum* dominated pixels by extrapolating the atmospheric reflectances derived through the 1st and 2nd steps over the *Sargassum*-free pixels that are located in the vicinity of the *Sargassum* contaminated pixel. Finally, the satellite reflectance measured over the *Sargassum* contaminated pixel is corrected for the atmosphere to provide the sea surface reflectance. The OLCI surface derived reflectance image after atmospheric correction is obtained for 12 spectral bands between 400 nm and 865 nm.

2.3.2. Sargassum Radiative Transfer (SRT) Model

As mentioned Section 1, the adaptation of the Lee semi-analytical radiative transfer model [20] proposed by Descloitres et al. [21] to account for the immersion of *Sargassum* aggregations is used here; such a model is further called *Sargassum* Radiative Transfer (and noted SRT). Similar to the Lee's model, SRT can simulate the above surface reflectance using the bio-optical properties of the water column, the bottom depth and bottom composition as inputs (forward model). More precisely, the inputs typically consist of the chlorophyll concentration (Chl), the Non-Algal Particles (NAP) concentration, and the Colored Dissolved Organic Matter (CDOM) absorption coefficient. These parameters determine the Inherent Optical Properties (IOP) of the water such as the absorption (a(λ)) and backscattering ($b_b(\lambda)$) coefficients that are used to model the deep-water reflectance $\rho_{rs}^{dp}(\lambda)$. Lee's model also considers the seabed reflectance and depth (z). In addition to Lee's model, SRT is also able to consider the depth and the fraction coverage (FC) of *Sargassum* as inputs [21]. To do that, the *Sargassum* aggregation is assumed as an opaque layer at a given depth z (at the surface or in-water). Such an opaque layer can be optically considered as a seafloor that would be solely composed of *Sargassum*. The seabed reflectance used in the Lee's model can, thus, be considered as a linear mixing between the immersed *Sargassum* reflectance ($\rho_{sargassum}(\lambda)$) and the *Sargassum*-free water reflectance ($\rho_w(\lambda)$). The seabed reflectance in Lee's model is replaced by the composite reflectance of the immersed *Sargassum* aggregation, noted $\rho_c(\lambda)$ (Equation(4)):

$$\rho_c(\lambda) = FC \times \rho_{sargassum}(\lambda) + (1 - FC) \times \rho_w(\lambda) \quad (4)$$

The reflectance of the water column for the layer that is in between the surface and the *Sargassum* aggregations at the depth z is noted $\rho_{rs}W$ and the reflectance of the *Sargassum* aggregations that are located at the depth z is noted $\rho_{rs}C$. These reflectances are expressed in Equations (5) and (6):

$$\rho_{rs}W(0^-, \lambda) = \rho_{rs}^{dp}(\lambda)\left(1 - e^{-\left(\frac{1}{\cos(\theta_w)} + \frac{D_u^W(\lambda)}{\cos(\theta_v)}\right)K_d(\lambda)z}\right) \quad (5)$$

$$\rho_{rs}C(0^-, \lambda) = \frac{1}{\pi}\rho_c(\lambda).e^{-\left(\frac{1}{\cos(\theta_w)} + \frac{D_u^C(\lambda)}{\cos(\theta_v)}\right)K_d(\lambda)z} \quad (6)$$

where Du^W and Du^C are the optical path-elongation factors for photons scattered by the water column and *Sargassum* aggregations respectively. θ_w and θ_v are the solar and

viewing zenith angle, respectively, and K_d is the diffuse attenuation coefficient. The sea water reflectance just beneath the surface ($\rho_{rs}(0^-, \lambda)$) is then the sum of $\rho_{rs}W$ and $\rho_{rs}C$. Finally, the above water reflectance $\rho_w^+(\lambda)$ is derived as follows (Equation (7)):

$$\rho_w^+(\lambda) = \frac{0.52\ \rho_{rs}(0^-, \lambda)}{1 - 1.56\ \rho_{rs}(0^-, \lambda)} \times \pi \quad (7)$$

The components of the SRT model that include the water parameters (Chl, NAP and CDOM) and the Fractional Coverage and depth of the *Sargassum* aggregations are presented in Figure 3.

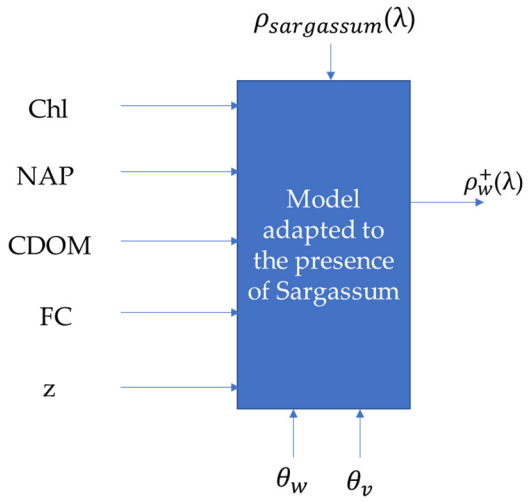

Figure 3. Inputs and output of the SRT model.

2.3.3. Inversion of the SRT Model to Retrieve the *Sargassum* Depth and Fractional Coverage

The inversion of the SRT model consists of using an optimization method to minimize the Euclidian distance between the sea surface reflectance that is derived from satellite observations and the simulated sea surface reflectance (forward SRT model). The bio-optical parameters (Chl, NAP, CDOM, FC, and z) for which the retrieved error between observations and simulations is minimum are selected.

The minimization is operated using the least squares method based on a first guess initial values of the bio-optical parameters, and on the range of variation of each parameter. The range of variation of the chlorophyll concentration was set between 0 and 2 mg m^{-3} based on the OCC-CI algorithm developed by the CMEMS (Copernicus European community) which provides monthly average of the chlorophyll-a in the Atlantic Ocean. The range of variation of the NAP concentration was set between 0 and 2 g m^{-3} and the CDOM absorption coefficient at 443 nm between 0 and 0.1 m^{-1}. These ranges of variation were set based on the S3W OLCI Level-2 products (distributed by EUMETSAT-CODA service) where the NAP ranged from 0.13 and 0.32 g m^{-3} and the CDOM from 0.04 and 0.06 m^{-1}. The FC ranges between 0 and 1 and z ranges from the surface (i.e., 0 m) to 5 m deep because *Sargassum* aggregations are known to float between 0 and 5 m [18,30–32]. The initial value of the bio-optical parameters was fixed as a first guess as follows: Chl = 0.5 mg m^{-3}, NAP = 1 g m^{-3}, CDOM = 0.0005 m^{-1}, FC = 1 and z = 0 m. The minimization process is stopped when the error between observations and simulations is below a threshold, namely 10^{-20}. Such threshold is relevant to overcome the issue of local minima. The five optimum parameters (Chl, NAP, CDOM, FC and z) are then estimated for each pixel of the satellite image. Practically, the MATLAB optimization function "*lsqcurvfit*" has been used.

2.3.4. Maximum Chlorophyll Index (MCI) and Fractional Coverage (FC)

The Maximum Chlorophyll Index MCI [11,13] is defined as follows (Equation (8)):

$$MCI = \rho'(709) - \left[\rho'(681) + (\rho'(754) - \rho'(681)) * \frac{709 - 681}{754 - 681}\right] \quad (8)$$

The MCI background (MCI_{bg}) value corresponds to the noise over *Sargassum* free waters. It can be estimated using a median filter window, which is efficient provided that a large majority of pixels inside this window is not contaminated by *Sargassum*. Our tests showed that a 167 × 167 pixels window (50 km × 50 km) is satisfactory to fulfill such a condition. MCI_{bg} is then subtracted from the MCI to derive the so-called MCI deviation, which is defined as $\delta MCI = MCI - MCI_{bg}$.

The fractional coverage can be linked to δMCI through a linear relationship δMCI = K*FC, where K is a coefficient of proportionality. K can be estimated using the SRT model outlined in Section 2.3.2 for a pixel that is entirely composed of *Sargassum*. K is equal to δMCI_{max} where δMCI_{max} is δMCI for a pixel composed only of *Sargassum* (i.e., FC = 100%) located at the surface (z = 0) [16]. In the current study, the value of K was estimated at 0.0579.

3. Results

3.1. Performances of the SRT Inversion Retrieval Process Using Synthetic Data

A synthetic dataset was generated to evaluate the performances of the SRT model inversion for retrieving particularly FC and z. For this purpose, the forward SRT model is used to simulate the surface reflectances for clear waters (i.e., Chl = 0.3 mg m^{-3}, NAP = 1 g m^{-3}, CDOM = 0.01 m^{-1}), with a depth z varying between 0 m and 5 m, and a fractional coverage varying between 0 and 1. The atmospheric effects are added to simulate the top of the atmosphere radiance using MODTRAN [33]. The OLCI instrumental features (i.e., spectral resolution and SNR) are then applied. In addition, an error representing the imperfect correction of atmospheric effects is taken into account. The minimization of the cost function is used to retrieve the water constituents, namely, Chl', NAP', CDOM', FC', and z'. The desired input parameters that were used to simulate the initial OLCI-like sea surface reflectances are then considered as the reference data to determine the error of the inversion approach. The performances of the SRT inversion retrievals are determined following the approach outlined in Figure 4.

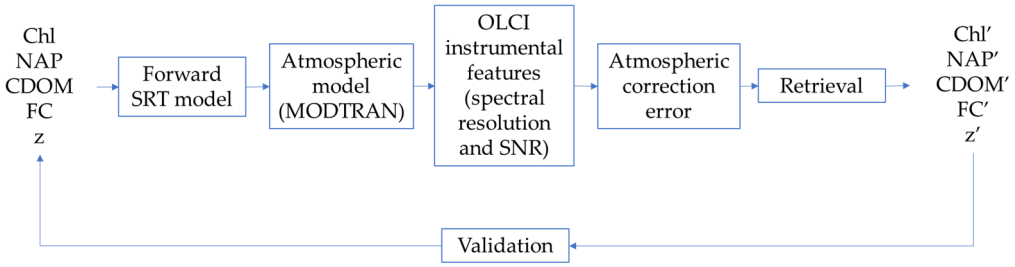

Figure 4. Flowchart describing the procedure used to determine the performances of SRT inversion retrievals.

The root mean square error (RMSE) and the relative RMSE (RRMSE) obtained between the parameters retrieved by the SRT inversion and the desired reference values of each parameter are reported Table 1. The retrieval error could be considered as satisfactory when the Relative RMSE is lower than 20% based on the current inversion algorithms performances [34]. Chl, NAP, and CDOM are retrieved with a weak RMSE. However, the retrievals of the Chl and CDOM parameters are not satisfactory as shown by their high RRMSE, which is greater than 45% and 70% for Chl and CDOM, respectively. The RRMSE estimated for the FC parameter is lower than 3%, thus indicating its good retrieval. Note

that a RMSE value for FC lower than 1% can be considered satisfactory even though it should be noted that *Sargassum* contaminated pixels typically show FC values lower than 5% [13]. The RRMSE value of 14.7% that is found for the parameter z, and its RMSE of 0.7 m are satisfactory.

Table 1. Performances of the SRT inversion retrieval of the bio-optical parameters in clear waters.

Parameters	$\mathbf{RMSE}=\sqrt{\frac{1}{N}\sum(\mathbf{C_{method}}-\mathbf{C_{reference}})^2}$	$\mathbf{RRMSE}=100*\mathbf{RMSE}\sqrt{\mathbf{C_{method}}}$
Chl (mg m^{-3})	0.14 mg m^{-3}	48.1%
NAP (g m^{-3})	0.13 g m^{-3}	13.4%
CDOM (m^{-1})	0.0078 m^{-1}	78.4%
FC (%)	1.51%	2.9%
z (m)	0.74 m	14.7%

Figure 5 shows the distribution of the relative RRMSE errors as a function of FC and z. In Figure 5, FC varies from 0 to 100% along the horizontal axis and z varies from 0 to 5 m along the vertical axis. Two large red bands could be observed in Figure 5d,e (one left vertical band and one top horizontal band, respectively) because the division by 0 (reference value) leads to infinity for RRMSE. The high values in Figure 5e in the left are due to the difficulty to estimate the depth for the case where there is no *Sargassum* occurrence (FC = 0). Figure 5 reveals that the deeper the *Sargassum* aggregation, the more difficult to correctly derive the fractional coverage and the depth (Figure 5d,e). Thereby, the inversion model performs better when the *Sargassum* aggregation is located close to the surface. Similarly, it is observed that the retrieval of FC parameter is more challenging (RRMSE > 15%, Figure 5d) when the depth is higher than 4 m (Figure 5d). The contribution of Chl, NAP, and CDOM is difficult to estimate for the case where the pixel is both covered by 100% of *Sargassum* (FC = 100%) and located near the surface (z = 0). This is because the surface reflectance is not influenced by hydrosols for such conditions.

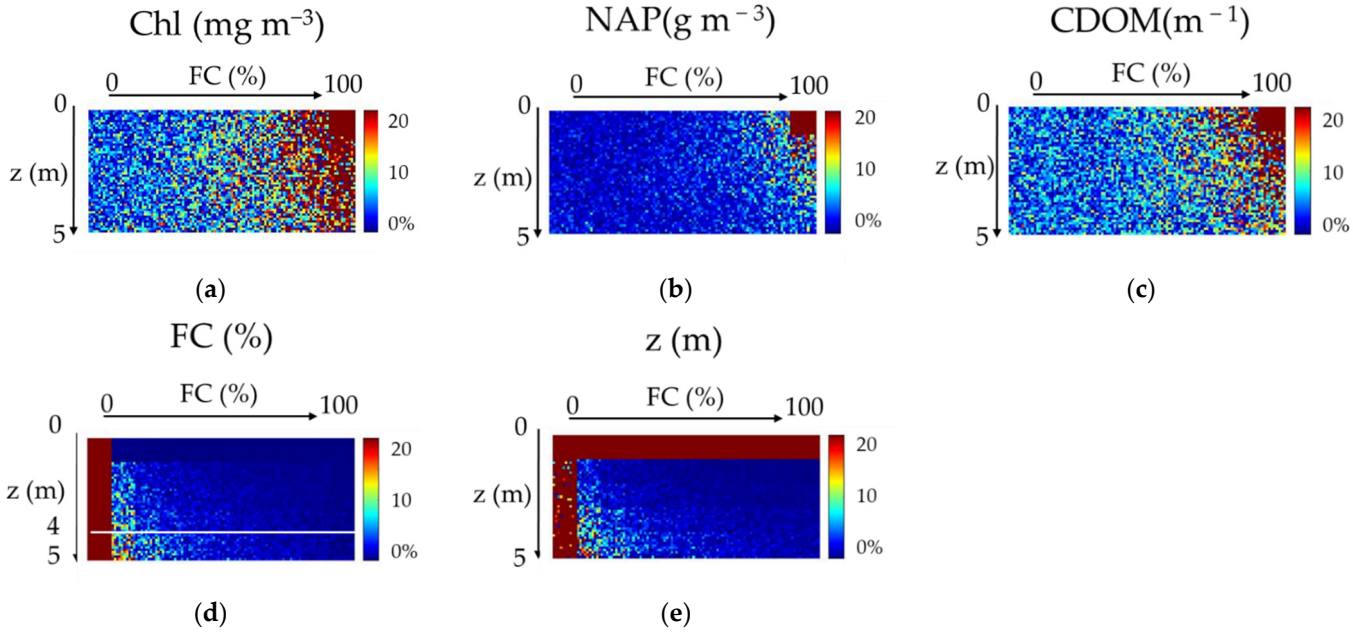

Figure 5. Relative error (RRMSE) of each bio-optical parameters retrieved using the SRT inversion method: FC varies on the horizontal axis from 0 to 100% and depth z varies on the vertical axis from 0 to 5 m. (**a**) Chlorophyll (Chl), (**b**) Non-Algal Particle (NAP), (**c**) Colored Dissolved Organic Matter (CDOM), (**d**) Fractional Coverage (FC), (**e**) Depth (z).

3.2. Retrieval of the Bio-Optical Parameters from OLCI Derived Surface Reflectances Using the SRT Inversion Method

Here, the SRT inversion method is applied to OLCI derived surface reflectances data acquired on 8 July 2017, in the study area as described Section 2.2 (white square in Figure 2). First, the results of the retrievals are shown for two types of pixels. One type of pixels contains only clear oceanic waters, i.e., *Sargassum*-free pixel, while the other type of pixel contains a mixing of seawater and *Sargassum* (i.e., *Sargassum* contaminated pixel). This last type of pixel was identified using the MCI index to ensure the presence of *Sargassum*. Table 2 summarizes the values of the retrieved parameters for a pixel of each type. Chl is estimated around 0.4 mg m^{-3} for both pixels; such a value matches with the range provided by the OC-CCI database near Dominica Island (i.e., 0.2–0.8 mg m^{-3}) in July 2017 [35]. For the case of a given pixel contaminated by *Sargassum*, FC and z values are consistent with the occurrence of a *Sargassum* aggregation close to the surface (8% of fractional coverage and 0.07 m depth). The FC value evaluated using the MCI index for the same pixel is 10%, which is close to the one estimated by the SRT inversion. The FC value estimated for the *Sargassum*-free pixel is 15%, which is not consistent since a value of FC of 0% should be theoretically retrieved when a pixel is not contaminated by *Sargassum*. The depth value retrieved for a *Sargassum*-free pixel is exactly 5 m. The SRT model should theoretically retrieve an infinite depth when a *Sargassum* aggregation is not present; however, the influence of the *Sargassum* on the surface reflectance decreases with increased depth. When *Sargassum* are located at 5 m depth, the difference between reflectance of *Sargassum*-free pixel and reflectance of pixel containing 10% of *Sargassum* that has been calculated using the SRT forward model is only 2%. Therefore, the maximum *Sargassum* depth for which our method is applicable is 5 m. It should be highlighted that previous studies [18,30–32] showed that the *Sargassum* community occupies the upper water column (up to 4 m depth). The pixels for which the retrieved depth reaches the maximum value (5 m) are further considered as *Sargassum*-free pixels (FC = 0%).

Table 2. Retrieved values of the bio-optical parameters estimated by the SRT inversion method for a *Sargassum*-free pixel and a *Sargassum* contaminated pixel for the OLCI data acquired on 8 July 2017.

Parameters	Retrieval for a *Sargassum* Free Pixel	Retrieval for a *Sargassum* Contaminated Pixel
Chl (mg m^{-3})	0.41	0.45
NAP (g m^{-3})	0.243	0.26
CDOM (m^{-1})	0.025	0.02
FC (%)	15	8
z (m)	5	0.07

Figure 6 shows the above surface reflectance derived from the OLCI observation and the surface reflectance computed using the forward SRT model based on the bio-optical parameters retrieved from the SRT inversion scheme (Table 2). The simulated surface reflectance correctly matches with the OLCI surface derived reflectance for the *Sargassum* free pixel (Figure 6a). The SRT inversion retrieval is slightly less performant in the blue domain (412 nm), where the relative error is 9% when comparing to the OLCI surface derived reflectance. The simulated reflectance corresponding to the SRT inversion retrieval for the *Sargassum* contaminated pixel also correctly agrees with the OLCI reflectance surface; the maximum relative error is 12% at 754 nm (Figure 6b).

The spatial distribution of the bio-optical parameters retrieved by the SRT inversion scheme over the study area (white square in Figure 2) is shown Figure 7. Land pixels are colored in grey, and clouds are colored in white. The Chl, NAP, and CDOM distributions are homogeneous within the study area (respectively Figure 7a–c). The spatial distribution of the retrieved parameters (Figure 7a–c) can be compared with Level-2 data products provided by the Copernicus data center for the same date and location. The retrieved Chl values range between 0.1 and 0.6 mg m^{-3}, which is highly consistent with the Level-2

product values that ranges from 0.2 to 0.8 mg m^{-3}. The retrieved NAP values range between 0.4 and 1.4 g m^{-3}, which is overestimated in comparison with the Level-2 product values that ranges from 0.13 to 0.32 g m^{-3}. The retrieved CDOM values range between 0.02 and 0.05 m^{-1}, which is fairly consistent with the Level-2 product values that ranges from 0.04 to 0.06 m^{-1}. The retrieved FC values range from 0 to 47% (Figure 7d). The retrieved depth values range from 0 to 5 m (Figure 7e). The pixels of the study area for which the retrieved depth reaches 5 m are considered as *Sargassum*-free pixel as explained in Section 3.1. Their associated FC values will further be discarded. Here, the presence of *Sargassum* can be found in areas for which z is lower than 4.9 m, typically between 15°30′N–61°45′W and 15°15′N–61°30′W (Figure 7e). Around 15°30′N and 61°15′W, FC is higher than 30%, and the related depth reaches 2.5 m. Note that such an area is influenced by the mouth of the Layou river (western Dominica Island). It is likely that the high-water turbidity induced by the river discharge leads to the failure of the model; the area is wrongly identified as *Sargassum* dominated. Note that turbid coastal zones might be discarded by extending a land-mask to the nearby coastal waters.

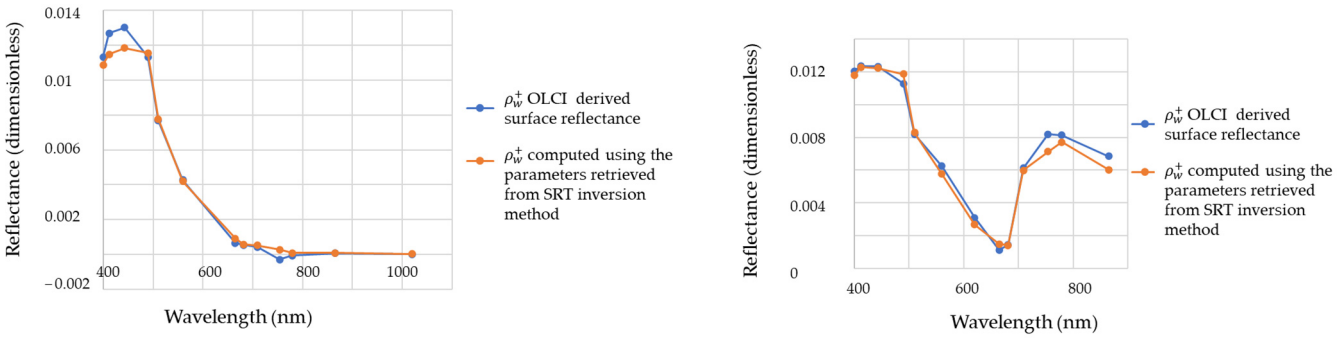

Figure 6. OLCI derived surface reflectance $\rho_\omega{}^+$ and computed surface reflectance using the retrieved bio-optical parameters from SRT inversion: (**a**) for a *Sargassum*-free pixel and (**b**) for a *Sargassum* contaminated pixel.

The retrieved FC and z values are filtered out to discard pixels corresponding to a depth higher than 4.9 m and a FC lower than 0.1% to visualize the *Sargassum* aggregations in the study area (Figure 8). Land/ocean borders are contoured in black. The FC values range from 0.1% to 39%. The *Sargassum* coverage of the area of interest can be estimated using the FC retrieval and the size of a OLCI pixel (0.3 × 0.3 km). The coverage area of *Sargassum* is then estimated to be 19.86 km^2 over the total 22,500 km^2 study area. FC tends to be higher in the center of the aggregations than on their edges (Figure 8a), which is consistent with the fact that the *Sargassum* could be more dispersed at the edges of the aggregations due to the water mixing.

About 80% of the retrieved depths are located between 1 m and the surface. The remaining 20% left is then retrieved between 1 and 4.9 m. The greater depths (z > 1 m) seem to be retrieved on the edges of the aggregations while the shallow depths (z < 1 m) are observed in the center of the aggregations (Figure 8b). This could be explained by the fact that the abundance of *Sargassum* is lower on the edges of the aggregations, and thus the *Sargassum* buoyancy is decreased.

The retrieval of FC is also performed using the δMCI approach. Note that the values retrieved by such a method for which FC is lower than 0.1% were filtered out; thus, the isolated pixels are discarded to prevent false detections. The comparison between δMCI and SRT inversion approaches is performed using a histogram (Figure 9). The histogram shows that FC values greater than 5% have more occurrences when using the SRT inversion (in red in Figure 9) than when using the δMCI approach (in blue in Figure 9). On the contrary, the FC values lower than 5% have more occurrences when using the δMCI approach than the SRT method. The relative increase in the *Sargassum* fractional coverage is estimated

to be 31% over the entire study area when using the SRT method in comparison to the δMCI method. Such an increase is due to the consideration of the immersion depth in the inversion process as outlined in this study. Therefore, the proposed methodology should retrieve a more realistic estimate of the FC values than the δMCI index.

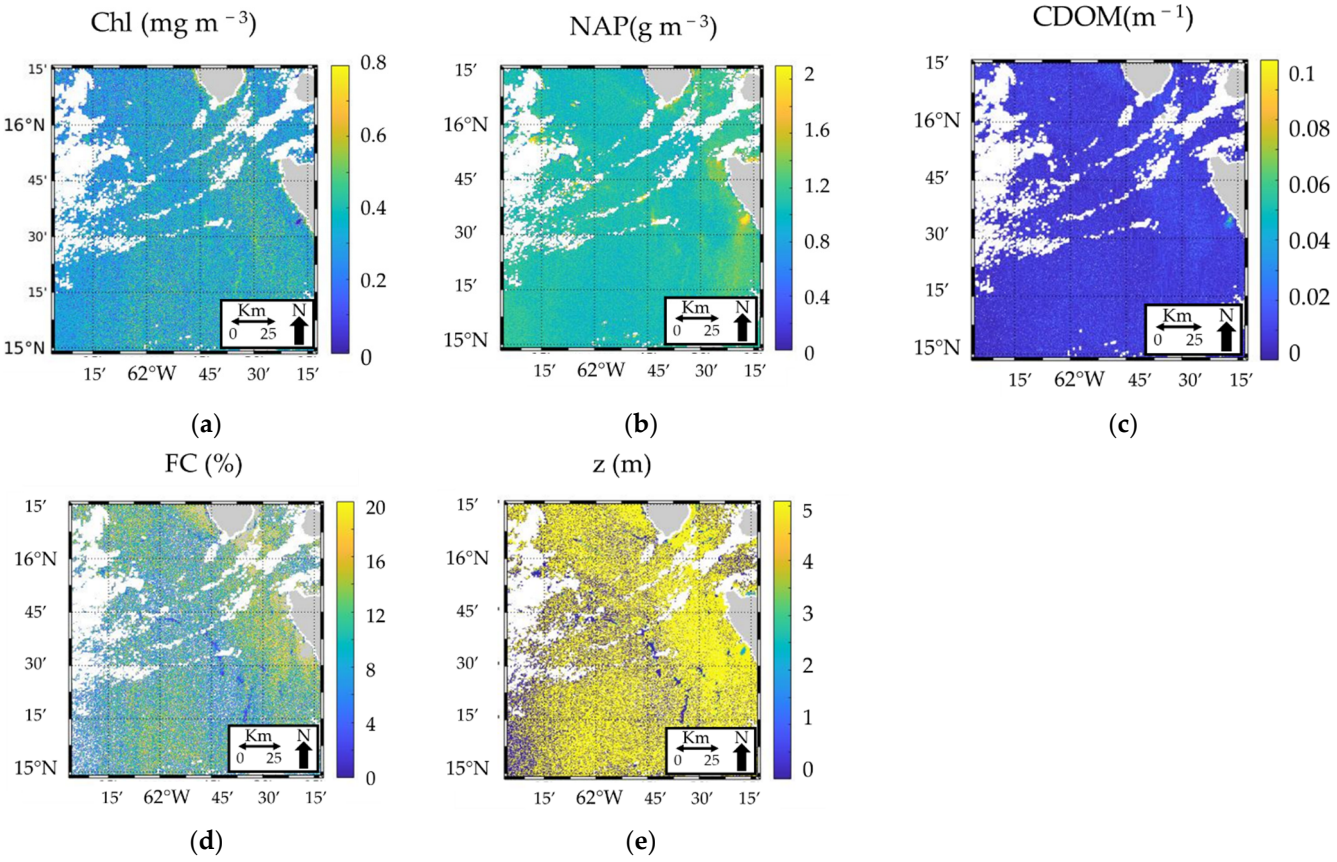

Figure 7. Spatial distribution of the bio-optical parameters retrieved by the SRT inversion applied to OLCI data acquired on 8 July 2017 over the study area (white square in Figure 2).

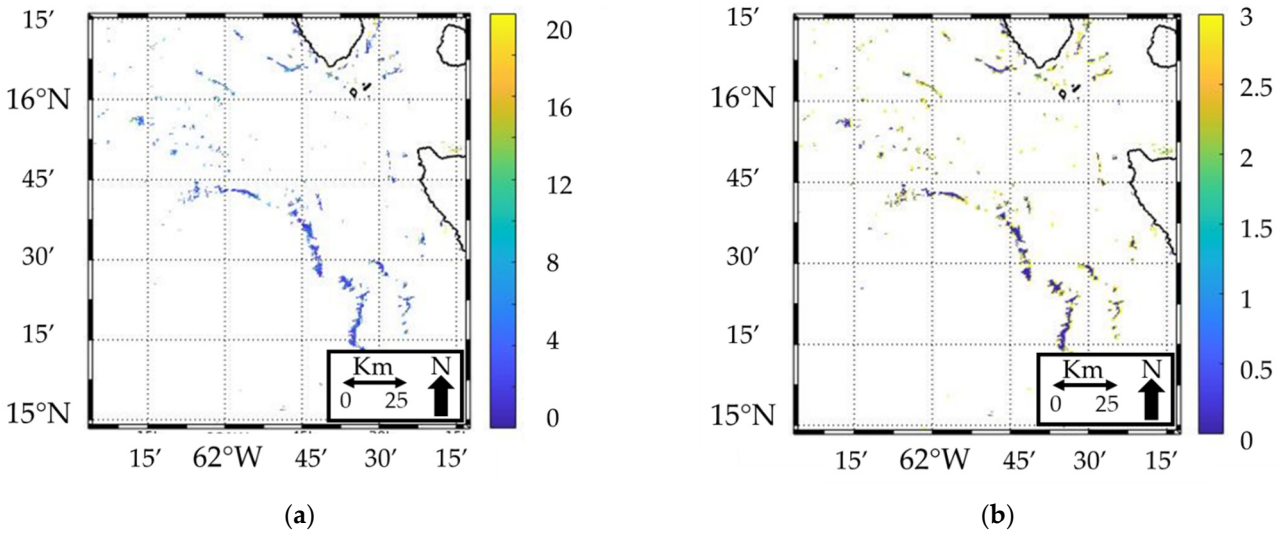

Figure 8. Spatial distribution of (**a**) FC (%) and (**b**) z retrieved by the SRT inversion method applied to the OLCI data acquired on 8 July, 2017, over the study area. Note that the data for which FC is lower than 0.1% and/or the depth is higher than 4.9 m were filtered out.

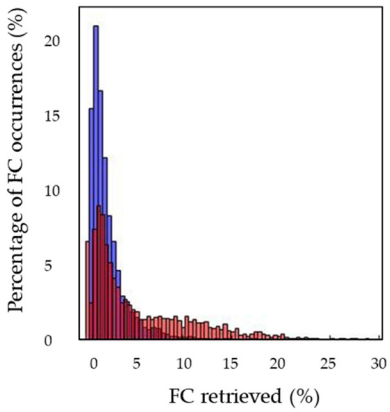

Figure 9. Histogram of the probability of occurrence (in %) of FC (in %) retrieved by the SRT inversion method (red) and by the δMCI (blue) for the study area of the scene acquired on 8 July 2017.

4. Neural Network Implementation to Speed-Up Satellite Data Processing

The SRT inversion approach uses an optimization method that is applied pixel by pixel, which can be highly time consuming. As an example, the processing of the study area (500 × 500 pixels) could take 1 h10 for computational time. The hardware used to estimate the computational time is an intel Core i7 processor, 2.60 Ghz × 12 CPU and 31 Gio RAM. Thus, the processing of an OLCI typical scene (4090 × 4865 pixels) would require about 10 days to retrieve the bio-optical parameters. A neural network approach was then implemented to reduce the computational time and to make more operational the application of the proposed method at larger scale. Neural network techniques have been previously implemented to detect the presence of *Sargassum* in the open ocean [16,17]; their training phase, which consists in recognizing *Sargassum* using spectral and spatial features, is performed using either the application of indexes such as AFAI and MCI. Neural networks can detect the presence of *Sargassum* and/or assess their abundance per pixels. However, they are not able yet to consider the *Sargassum* immersion depth. Here, the neural network was trained using a simulated dataset because in situ data of the immersion depth of the *Sargassum* aggregation are not available. The forward SRT model was used to create such a training dataset which links the bio-optical parameters to their associated surface reflectances. A noise is added to the simulated surface reflectances using the same method as described Section 3.1 to obtain OLCI-like surface reflectances. The artificial neural network is trained to estimate the five bio-optical parameters (Chl, NAP, CDOM, FC and z) from the simulated OLCI-like surface reflectances (12 spectral bands). It is then able to perform the inversion of the SRT model for the OLCI surface derived reflectances image, pixel by pixel. The artificial neural network is based on a multi-layer perceptron model (MLP) which enables to approximate non-linear functions to estimate continuous outputs [36].The neural network was built using 4 hidden layers of 50 neurons fully connected (Figure 10a). The training phase, the test phase, and the validation phase were applied using, respectively, 70%, 15%, and 15% of the dataset. The training phase duration is 12 h when using 100,000 samples composed by the set of reflectances and associated water constituents. It should be highlighted that the training phase is performed only once. Then, the neural network can be applied to any OLCI scene within a few minutes, thus significantly decreasing the computational time. The metric used to evaluate the learning performances for each phase (training, test, and validation) is the mean squared error (MSE) which is expressed as follows (Equation (9)):

$$\mathrm{MSE} = \frac{1}{\mathrm{N}} \sum (\mathrm{C}_{\mathrm{reference}} - \mathrm{C}_{\mathrm{estimation}})^2 \quad (9)$$

where N is the number of evaluated parameters for each phase. One epoch is defined as one training cycle for which the dataset is processed by the algorithm. The variation of the MSE with the epoch number for each step of the learning process (training, test, and

validation phase) is shown Figure 10b. A similar shape is observed for the training and the test phase. The epoch number for which MSE of the test phase is minimum points out the number of training cycle that is sufficient for stopping the learning process. Here, the value of this epoch number is 42. The learning process could lead to overfitting of a given neural network when MSE for the validation phase increases with respect to the epoch number prior to that of the MSE for the test phase. Since the MSE for both the test and validation phases starts to increase for the same epoch number, namely, 42 (Figure 10b), the neural network proposed here does not show any overfitting issues. The error on the FC component (Figure 10c) mostly ranges between −3% and +3%, which is satisfactory (i.e., lower than 1%). The error on z (Figure 10d) is also satisfactory since the histogram, which is centered on the value 0, rapidly decreases beyond +0.5 m, and below −1 m. The performances of the neural network are also evaluated using a different and larger dataset than the one used during the learning process (the approach has been described in Section 3.1). The RMSE values are 0.3 mg m^{-3} for Chl, 0.21 g m^{-3} for NAP, 0.006 m^{-1} for CDOM, 3.1% for FC, and 0.54 m for z. These RMSE values are close to those obtained previously when using the SRT inversion approach (Table 1).

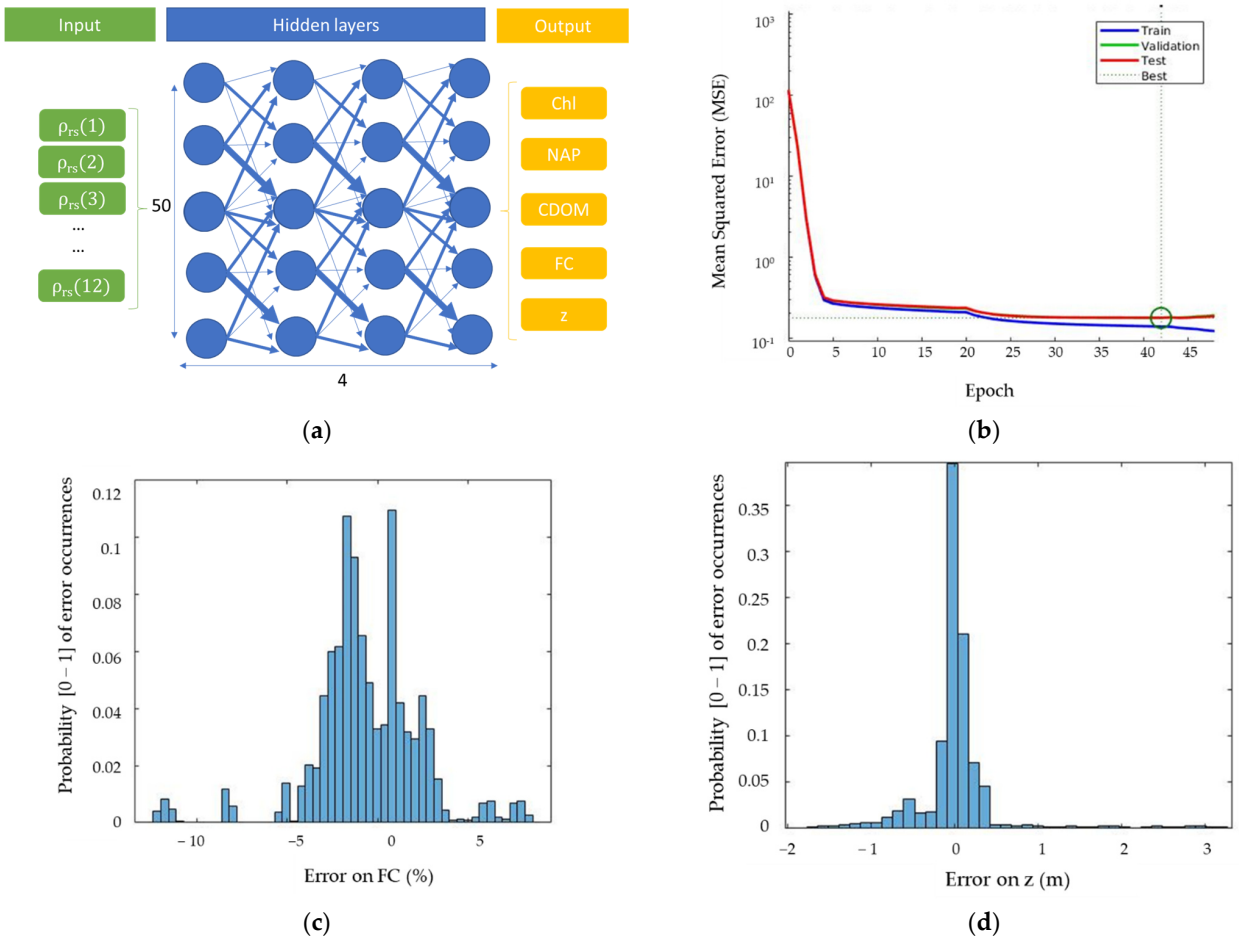

Figure 10. (**a**) Neural Network Architecture; (**b**) MSE per epoch for the training phase (blue), validation phase (green) and test phase (red); the histogram of the probability of the error (validation phase) (**c**) for FC component and (**d**) for z component.

The neural network is then applied to OLCI derived surface reflectances using the study area (white square Figure 2) of the scene acquired on 8 July 2017. The spatial variation of the fractional coverage and the immersion depth of the *Sargassum* aggregations are examined (Figure 11). The spatial distribution of FC is shown in Figure 11a for which FC values lower than 0.1%. Beyond 5 m depth, the *Sargassum* occurrence does not sufficiently

influence the sea surface total reflectance to properly enable their identification (Section 3.2). In addition, previous studies showed that *Sargassum* are mostly found in the upper water column (from the surface to 4 m depth) [18,30–32]. Then, FC is not determined in this study for depth values greater than 4.9 m. The same main aggregation patterns are detected when using the neural network (Figure 11a) relatively to the SRT inversion. The estimated z component appears lower when using the neural network approach (<2.5 m) (Figure 11b) relatively to the SRT inversion (Figure 8b), especially on the edges of the aggregations (about 3 m when using the SRT inversion). The variation of the depth retrieval within the *Sargassum* aggregations is fairly smooth when using the neural network relatively to the SRT depth retrieval which exhibits a sharp increase on the edges of the aggregations.

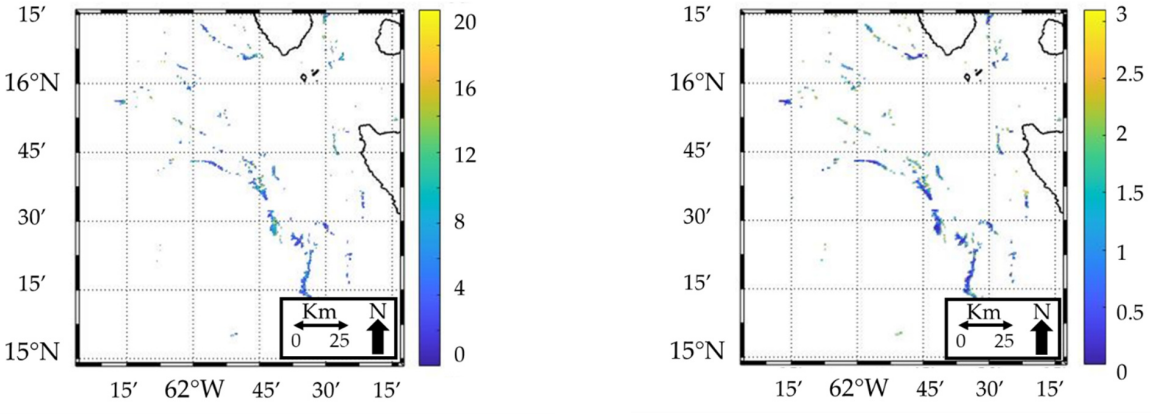

(**a**) (**b**)

Figure 11. Spatial distribution of (**a**) FC (%) and (**b**) z retrieved by the neural network approach applied to the OLCI data acquired on 8 July 2017, over the study area (white square in Figure 2). Note that the data for which FC is lower than 0.1% and/or the depth is higher than 4.9 m were filtered out.

The neural network is then applied to the entire scene acquired on 8 July 2017. FC retrievals range from 0.1% to 34% over the entire area. The proportion of *Sargassum* occurrences as a function of depth is shown Figure 12b. The highest number of occurrences is observed between 0 and 0.5 m. More interestingly, about 80% of the *Sargassum* are located in the depth range from 0.5 m to 4.9 m and 36% from 2 m to 4.9 m (Figure 12c), thus highlighting the great interest of considering immersed *Sargassum* in the inversion process.

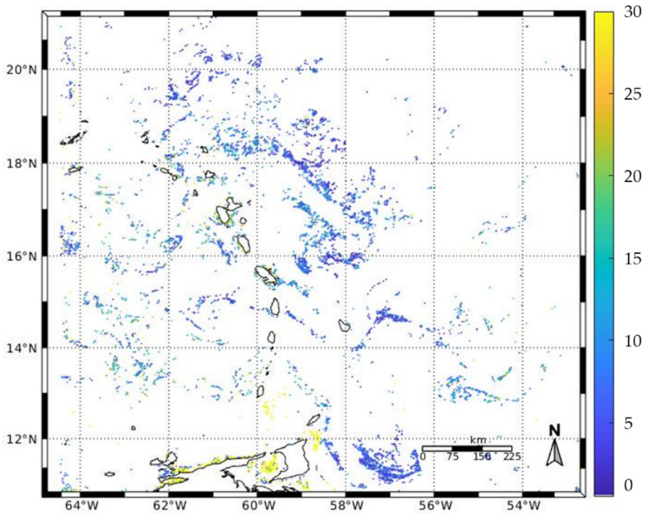

(**a**)

Figure 12. *Cont.*

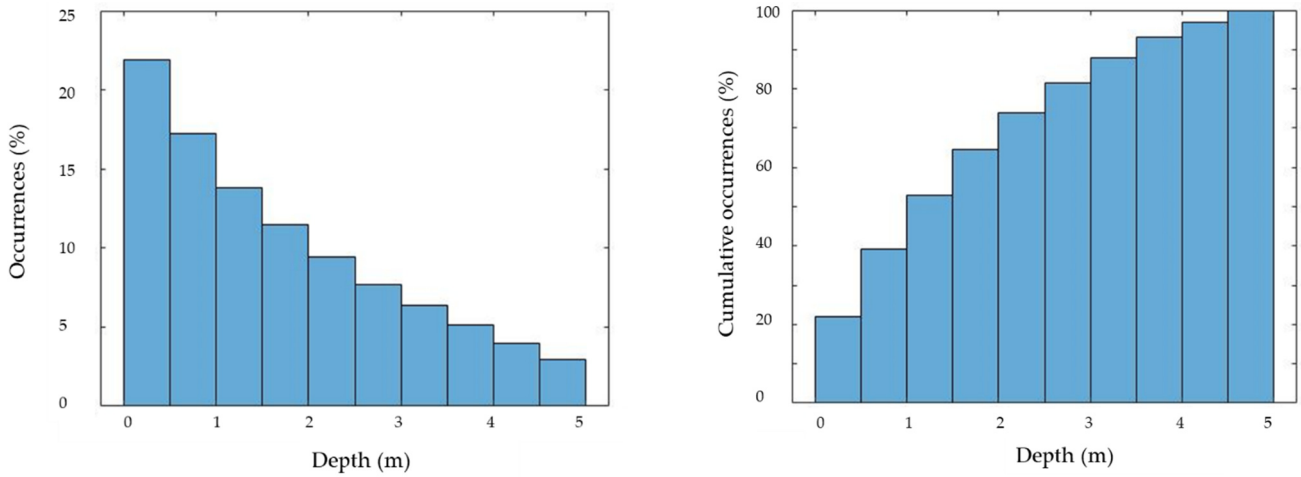

(**b**) (**c**)

Figure 12. (**a**) Spatial distribution of FC (color bar in %) retrieved by the neural network approach for the OLCI scene acquired on 8 July 2017; (**b**) histogram of the *Sargassum* occurrence (in %) and (**c**) cumulative histogram of the *Sargassum* occurrence (in %) of depth retrieved by the neural network.

5. Discussion

The retrieval of FC can also be carried out using the δMCI approach (Figure 13a). A comparison of the different approaches (δMCI and neural network) is also performed on the resulting OLCI image. It is observed that the neural network successfully detects most of the aggregations that were also identified from δMCI. However, the δMCI approach detects more *Sargassum* occurrences than the neural network approach in the north-east part of the scene. It may be caused by very thin clouds in this area, which could lead to an overestimation of the *Sargassum* occurrence by δMCI. A composite RGB image (Figure 13b) which focuses on the north-east part of the scene enables visualization of the thin clouds. The red circle in Figure 13a shows a *Sargassum* detection made by the δMCI approach that is likely to be a thin cloud based on Figure 13b (see red circle). More *Sargassum* contaminated pixels are retrieved in the center of the scene using the neural network when comparing to the δMCI approach. Even though the lack of in situ data prevents the validation of the additional *Sargassum* detections provided by the neural network approach, it should be highlighted that those additional occurrences are located in the vicinity of the main aggregation patterns that are already detected by the δMCI. The latter point corroborates the fact that the neural network retrievals are consistent with the current standard method. The additional detections are located around existing aggregations. The neural network approach indicates that 2.20% of the pixels of the entire OLCI scene are contaminated by *Sargassum* against 1.53% when considering the δMCI. The relative increase in the *Sargassum* coverage is, thus, 43% when using the neural network in comparison to δMCI approach. Such an increase could be explained by the fact that the neural network is able to take into account the depths of the aggregations. The retrieval of FC using MCI is based on the red and NIR reflectances where pure seawater strongly absorbs the light. The value of the pure seawater diffuse attenuation coefficient (noted K_{dw} in m^{-1}) at 681 nm is 0.45 m^{-1} [37]. Since about 90% of the radiation exiting the water column typically comes from a depth layer of $1/K_{dw}$, the boundary maximum depth for which *Sargassum* could be potentially detected from above water reflectance is, thus, not greater than 2 m. However, the physical approach proposed here relies on spectral reflectances ranging from the blue domain (400 nm) to the NIR. The fact that short wavelengths are taken into account in our approach enables increasing the depth layer for which *Sargassum* might be detected. The value of K_{dw} at 400 nm is 0.0209 m^{-1}, thus theoretically allowing observing a depth layer up to 48 m.

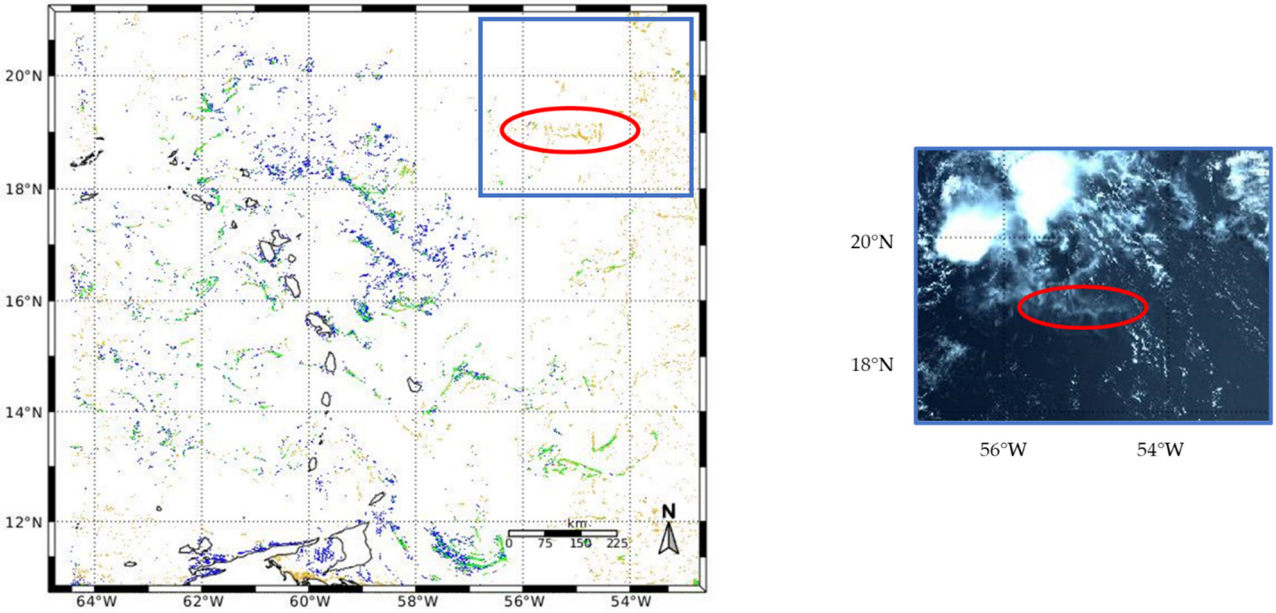

(**a**) (**b**)

Figure 13. (**a**) Spatial distribution of the *Sargassum* detections for the OLCI scene acquired on 8 July 2017, using the FC values retrieved by the neural network approach (blue), by the δMCI approach (yellow) and by both approaches (green); (**b**) RBG composite image of a regional area in the north-east corner of the OLCI scene.

The retrieval of FC and z values from the neural network and from δMCI (only FC for this latter index) has also been applied to other scenes of the dataset (Section 2.2). Table 3 summarizes the fractional coverage retrieved by both δMCI and neural network as well as the proportion of the coverage retrieved by the neural network between 2 m and 5 m depth. The coverage estimated using the neural network is higher by a factor of 2 than that derived using δMCI approach for all the scenes except for the scene acquired on 2 May 2021, for which the coverage is fairly similar for both methods. The relative increase in the coverage retrieval ranges from 0.7% to 68.6% for the scenes considered here when using the neural network in comparison to the current δMCI approach. The proportion of coverage estimated by the neural network between 2 m and 5 m ranges from 30% to 51%. The scene acquired on 2 May 2021, shows a relative coverage difference lower than 1% when using the neural network approach relatively to the δMCI approach (Table 3). Such a value can appear inconsistent relatively to the high percentage of estimation of immersed *Sargassum* (42% deeper than 2 m). However, it should be highlighted that the scene is highly impacted by clouds (about 60% of cloud coverage) which could lead to an overestimation of *Sargassum* FC by the δMCI approach. This is because the high coverage of clouds could prevent the correction of the median filtering window (Section 2.3.4). The δMCI approach detects more *Sargassum* occurrences in the east part of the scene. For such an area, the neural network approach does not detect the occurrence of *Sargassum*, which could explain the weak value of the relative coverage difference (<1%). However, it remains difficult to draw any conclusions about the best method that could estimate *Sargassum* occurrence as far as the acquisition of in situ data is lacking to validate the retrieved products. The IFREMER CERSAT Global Blended Mean Wind Fields is a database that is available from the Copernicus services CMEMS, which provides 6-hourly wind components including wind speed between 1992 and 2020 [38]. The spatial means of the wind provided for the area of interest are 5.5 m s^{-1} for 14 September 2020, and also for 28 December 2020; 6.5 m s^{-1} for 8 July 2017; and more than 7.2 m s^{-1} for 14 June 2020, and 27 May 2018. The scenes for which the wind speed is the highest (>6.5 m.s^{-1}) corresponds to the scenes where a higher coverage is estimated between 2 m and 5 m (>39% here). The wind speed

could then be potentially linked to the abundance of immersed *Sargassum* [29]. Previous observations also reported a relationship between the wind and the vertical mixing of *Sargassum*; the presence of *Sargassum* below the surface was particularly observed for strong wind conditions (i.e., >4 m s^{-1}) [19].

Table 3. Comparison of the *Sargassum* coverage (in km^2) estimated from the neural network and the δMCI approaches for the OLCI image dataset.

Date	Coverage (km^2) δMCI Index (Surface Waters Only)	Coverage (km^2) Neural Network (Surface + Water Column)	Relative Coverage Difference (in %) between the Neural Network and δMCI	Proportion (in %) of Coverage between 2–5 m Depth (Neural Network Approach)
8 July 2017	933.6	1666.0	43.9%	51%
27 May 2018	1207.3	3880.1	68.8%	39%
14 June 2020	558.6	1055.6	47.1%	44%
14 September 2020	1340.2	3674.1	63.5%	31%
28 December 2020	488.0	932.3	47.6%	30%
2 May 2021	1884.3	1871.5	0.6%	42%

According to the calibration constant of 3.34 kg m^{-2} proposed by Wang et al. [15], to convert the area of Sargassum (km^2) into total wet biomass (metric tons), the Sargassum coverage (km^2) that are outlined in Table 3 for the δMCI and the neural network approaches can be converted into Sargassum biomass (Million tons) for the various OLCI scenes (Table 4). It is interesting to note that the derived Sargassum biomass values roughly show the same order of magnitude as the biomass estimates performed by Wang et al. [15] in the Caribbean Sea and the central-west Atlantic region for July 2015 (4.4 million tons) and by Parr [39] for the Sargasso Sea (7–10 million tons), bearing in mind that the Sargassum area coverage differ between their satellite dataset and the dataset used in this study.

Table 4. Comparison of the *Sargassum* biomass (in million tons) derived from both the δMCI and the neural network approaches for the OLCI image dataset.

Date	Biomass (Million Tons)	
	δMCI Index (Surface Waters Only)	Neural Network (Surface + Water Column)
8 July 2017	3.1	5.6
27 May 2018	4.0	13.0
14 June 2020	1.9	3.5
14 September 2020	4.5	12.3
28 December 2020	1.6	3.1
2 May 2021	6.3	6.3

6. Conclusions

The current methods used for the detection of *Sargassum* aggregations from satellite data over open ocean waters rely on spectral reflectance indexes (e.g., MCI index) that emphasize the *Sargassum* optical signature in the red-edge and the near infrared bands. However, since the water strongly absorbs in the NIR domain, those indexes are ineffective when the *Sargassum* are immersed in the water column. The semi-analytical radiative transfer model developed by Lee et al. [20] has been recently adjusted to take into account *Sargassum* contaminated pixels for which the aggregations could be located at a given immersion depth z [16]. Such an adapted model was referred here as SRT model. The originality of this study is to invert the surface reflectance as derived from satellite data using the SRT model to retrieve the bio-optical parameters such as the *Sargassum* aggregation features (FC and z). The inversion is carried out using an optimization process between the OLCI derived surface reflectance and the simulated surface reflectance from the forward version of the SRT model.

The performances of the SRT inversion retrieval were first estimated using a simulated dataset since in situ data were not available. Typically, the RMSE values were lower than 1% for FC and about 0.54 m for z, which is satisfactory. The proposed approach was then applied to Sentinel-3/OLCI sensor data. A relative increase of 31% in *Sargassum* coverage was found when comparing to the coverage that is currently estimated using the MCI algal index. It was shown that the aggregations are located deeper in the water column at the edge of their spatial area while their fractional coverage (or abundance) is weaker. The inversion process that relies on the SRT physical model is highly time consuming, typically about 10 days for a typical OLCI image (4090 × 4865 pixels); therefore, a neural network approach was used to make more operational the application of the proposed method to a large dataset. The neural network was trained using a synthetic dataset. Seven Sentinel-3/OLCI scenes that were acquired at various years and seasons were examined. The *Sargassum* coverage retrieved by the neural network was about two times higher than that retrieved using the MCI approach for six out of seven scenes. The retrieval of the *Sargassum* depth showed that between 30% and 51% of the estimated depth are located between 2 m and 5 m. The consideration of the depth is then a relevant parameter that should clearly be taken into account for the estimation of the *Sargassum* abundance in the open ocean. The approach proposed here could also be useful in time series analysis for providing a more reliable tracking of the aggregations. Note that other types of deep learning techniques could be searched in addition to the neural network to improve the overall processing and to provide a better understanding of the aggregation's characteristics. Further work could consist in using the methodology proposed here to improve strandings forecast by considering the immersed *Sargassum* and their depth locations in the forecast models.

Author Contributions: Conceptualization, A.M.; Data curation, L.S.; Formal analysis, L.S. and M.C.; Funding acquisition, A.M.; Methodology, A.M. and M.C.; Software, L.S.; Supervision, A.M.; Writing—original draft, L.S.; Writing—review and editing, A.M. and M.C. All authors have read and agreed to the published version of the manuscript.

Funding: This research was funded by l'Agence Nationale de la Recherche (France), grant number ANR-19-SARG-0007-07 and the Programme National de Télédétection Spatiale (PNTS, grant No. PNTS-2023-03).

Institutional Review Board Statement: Not applicable.

Informed Consent Statement: Not applicable.

Data Availability Statement: Not applicable.

Conflicts of Interest: The authors declare no conflict of interest.

References

1. Louime, C.; Fortune, J.; Gervais, G. Sargassum Invasion of Coastal Environments: A Growing Concern. *Am. J. Environ. Sci.* **2017**, *13*, 58–64. [CrossRef]
2. Gower, J.; Young, E.; King, S. Satellite Images Suggest a New Sargassum Source Region in 2011. *Remote Sens. Lett.* **2013**, *4*, 764–773. [CrossRef]
3. Jouanno, J.; Moquet, J.-S.; Berline, L.; Radenac, M.-H.; Santini, W.; Changeux, T.; Thibaut, T.; Podlejski, W.; Ménard, F.; Martinez, J.-M.; et al. Evolution of the Riverine Nutrient Export to the Tropical Atlantic over the Last 15 Years: Is There a Link with Sargassum Proliferation? *Environ. Res. Lett.* **2021**, *16*, 034042. [CrossRef]
4. Milledge, J.J.; Harvey, P.J. Golden Tides: Problem or Golden Opportunity? The Valorisation of Sargassum from Beach Inundations. *J. Mar. Sci. Eng.* **2016**, *4*, 60. [CrossRef]
5. Duncan, R.S.; Wilson, E.O. *Southern Wonder: Alabama's Surprising Biodiversity*; University of Alabama Press: Tuscaloosa, AL, USA, 2013.
6. Djakouré, S.; Araujo, M.; Hounsou-Gbo, A.; Noriega, C.; Bourlès, B. On the Potential Causes of the Recent Pelagic Sargassum Blooms Events in the Tropical North Atlantic Ocean. *Biogeosci. Discuss.* **2017**, 1–20. [CrossRef]
7. Marx, U.C.; Roles, J.; Hankamer, B. Sargassum Blooms in the Atlantic Ocean—From a Burden to an Asset. *Algal Res.* **2021**, *54*, 102188. [CrossRef]
8. Gower, J.; King, S.; Yan, W.; Borstad, G.; Brown, L. Use of the 709 Nm Band of MERIS to Detect Intense Plankton Blooms and Other Conditions in Coastal Waters. In Proceedings of the MERIS User Workshop, Frascati, Italy, 10–13 November 2003; pp. 10–13.

9. Gower, J.; Hu, C.; Borstad, G.; King, S. Ocean Color Satellites Show Extensive Lines of Floating Sargassum in the Gulf of Mexico. *IEEE Trans. Geosci. Remote Sens.* **2006**, *44*, 3619–3625. [CrossRef]
10. Hu, C.; Feng, L.; Hardy, R.F.; Hochberg, E.J. Spectral and Spatial Requirements of Remote Measurements of Pelagic Sargassum Macroalgae. *Remote Sens. Environ.* **2015**, *167*, 229–246. [CrossRef]
11. Gower, J.; King, S. The Distribution of Pelagic Sargassum Observed with OLCI. *Int. J. Remote Sens.* **2020**, *41*, 5669–5679. [CrossRef]
12. Hu, C. A Novel Ocean Color Index to Detect Floating Algae in the Global Oceans. *Remote Sens. Environ.* **2009**, *113*, 2118–2129. [CrossRef]
13. Wang, M.; Hu, C. Mapping and Quantifying Sargassum Distribution and Coverage in the Central West Atlantic Using MODIS Observations. *Remote Sens. Environ.* **2016**, *183*, 350–367. [CrossRef]
14. Gower, J.; King, S. Intense Plankton Blooms and Sargassum Detected by MERIS. In Proceedings of the MERIS (A) ATSR Workshop 2005, Frascati, Italy, 26–30 September 2005; Volume 597.
15. Wang, M.; Hu, C.; Cannizzaro, J.; English, D.; Han, X.; Naar, D.; Lapointe, B.; Brewton, R.; Hernandez, F. Remote Sensing of Sargassum Biomass, Nutrients, and Pigments. *Geophys. Res. Lett.* **2018**, *45*, 12–359. [CrossRef]
16. Wang, M.; Hu, C. Satellite Remote Sensing of Pelagic Sargassum Macroalgae: The Power of High Resolution and Deep Learning. *Remote Sens. Environ.* **2021**, *264*, 112631. [CrossRef]
17. Arellano-Verdejo, J.; Lazcano-Hernandez, H.E.; Cabanillas-Terán, N. ERISNet: Deep Neural Network for Sargassum Detection along the Coastline of the Mexican Caribbean. *PeerJ* **2019**, *7*, e6842. [CrossRef] [PubMed]
18. Woodcock, A.H. Winds Subsurface Pelagic Sargassum and Langmuir Circulations. *J. Exp. Mar. Biol. Ecol.* **1993**, *170*, 117–125. [CrossRef]
19. Ody, A.; Thibaut, T.; Berline, L.; Changeux, T.; André, J.-M.; Chevalier, C.; Blanfuné, A.; Blanchot, J.; Ruitton, S.; Stiger-Pouvreau, V.; et al. From In Situ to Satellite Observations of Pelagic Sargassum Distribution and Aggregation in the Tropical North Atlantic Ocean. *PLoS ONE* **2019**, *14*, e0222584. [CrossRef]
20. Lee, Z.; Carder, K.L.; Mobley, C.D.; Steward, R.G.; Patch, J.S. Hyperspectral Remote Sensing for Shallow Waters. I. A Semianalytical Model. *Appl. Opt.* **1998**, *37*, 6329–6338. [CrossRef]
21. Descloitres, J.; Minghelli, A.; Steinmetz, F.; Chevalier, C.; Chami, M.; Berline, L. Revisited Estimation of Moderate Resolution Sargassum Fractional Coverage Using Decametric Satellite Data (S2-MSI). *Remote Sens.* **2021**, *13*, 5106. [CrossRef]
22. Donlon, C.; Berruti, B.; Buongiorno, A.; Ferreira, M.-H.; Féménias, P.; Frerick, J.; Goryl, P.; Klein, U.; Laur, H.; Mavrocordatos, C.; et al. The Global Monitoring for Environment and Security (GMES) Sentinel-3 Mission. *Remote Sens. Environ.* **2012**, *120*, 37–57. [CrossRef]
23. Copernicus Open Access Hub Website. Available online: https://scihub.copernicus.eu/ (accessed on 5 October 2021).
24. Qi, L.; Hu, C.; Mikelsons, K.; Wang, M.; Lance, V.; Sun, S.; Barnes, B.B.; Zhao, J.; Van der Zande, D. In Search of Floating Algae and Other Organisms in Global Oceans and Lakes. *Remote Sens. Environ.* **2020**, *239*, 111659. [CrossRef]
25. Steinmetz, F. Étude de La Correction de La Diffusion Atmosphérique et Du Rayonnement Solaire Réfléchi Par La Surface Agitée de La Mer Pour l'observation de La Couleur de l'océan Depuis l'espace. Ph.D. Thesis, Lille 1, Lille, France, 2008.
26. Steinmetz, F.; Deschamps, P.-Y.; Ramon, D. Atmospheric Correction in Presence of Sun Glint: Application to MERIS. *Opt. Express* **2011**, *19*, 9783–9800. [CrossRef] [PubMed]
27. Steinmetz, F.; Ramon, D. Sentinel-2 MSI and Sentinel-3 OLCI Consistent Ocean Colour Products Using POLYMER. In Proceedings of the Remote Sensing of the Open and Coastal Ocean and Inland Waters, Honolulu, HI, USA, 24–25 September 2018; Volume 10778, p. 107780E.
28. Cox, C.; Munk, W. Measurement of the Roughness of the Sea Surface from Photographs of the Sun's Glitter. *Josa* **1954**, *44*, 838–850. [CrossRef]
29. Schamberger, L.; Minghelli, A.; Chami, M.; Steinmetz, F. Improvement of Atmospheric Correction of Satellite Sentinel-3/OLCI Data for Oceanic Waters in Presence of Sargassum. *Remote Sens.* **2022**, *14*, 386. [CrossRef]
30. Winge, Ø. *The Sargasso Sea, Its Boundaries and Vegetation*; A.F. Høst & søn: Copenhagen, Denmark, 1923.
31. Johnson, D.L.; Richardson, P.L. On the Wind-Induced Sinking of Sargassum. *J. Exp. Mar. Biol. Ecol.* **1977**, *28*, 255–267. [CrossRef]
32. Butler, J.N.; Morris, B.F.; Cadwallader, J.; Stoner, A.W. *Studies of Sargassum and the Sargassum Community*; Bermuda Biological Station: Ferry Reach, Bermuda, 1983.
33. Xu, Y.; Wang, R.; Liu, S.; Yang, S.; Yan, B. Atmospheric Correction of Hyperspectral Data Using MODTRAN Model. In Proceedings of the SPIE, the International Society for Optical Engineering, Volume 7123, Remote Sensing of the Environment: 16th National Symposium on Remote Sensing of China, Beijing, China, 7–10 September 2007; p. 712306. [CrossRef]
34. Dekker, A.G.; Phinn, S.R.; Anstee, J.; Bissett, P.; Brando, V.E.; Casey, B.; Fearns, P.; Hedley, J.; Klonowski, W.; Lee, Z.P.; et al. Intercomparison of Shallow Water Bathymetry, Hydro-Optics, and Benthos Mapping Techniques in Australian and Caribbean Coastal Environments. *Limnol. Oceanogr. Methods* **2011**, *9*, 396–425. [CrossRef]
35. Wekeo Website Mass Concentration of Chlorophyll a in Sea Water. Available online: Https://www.Wekeo.Eu/Data/ (accessed on 7 May 2022).
36. Gardner, M.W.; Dorling, S. Artificial Neural Networks (the Multilayer Perceptron)—A Review of Applications in the Atmospheric Sciences. *Atmos. Environ.* **1998**, *32*, 2627–2636. [CrossRef]
37. Mobley, C.D. The Optical Properties of Water. In *Handbook of Optics*; McGraw-Hill, Inc.: New York, NY, USA, 1995; Volume 1, Chapter 43.

38. Wekeo Website, IFREMER CERSAT Global Blended Mean Wind Fields. Available online: Https://Www.Wekeo.Eu/Data?View=dataset&dataset=EO%3AMO%3ADAT%3AWIND_GLO_WIND_L4_REP_OBSERVATIONS_012_006 (accessed on 13 May 2022).
39. Parr, A.E. Quantitative Observations on the Pelagic Sargassum Vegetation of the Western North Atlantic. *Bull. Bingham Ocean. Coll.* **1939**, *6*, 1–94.